IOP Publishing Measurement Science and Technology
Meas. Sci. Technol. **31** (2020) 045902 (15pp) https://doi.org/10.1088/1361-6501/ab58e5

A GPU-based phase tracking method for planetary radio science applications

Nianchuan Jian[1], Dmitry Mikushin[2], Jianguo Yan[3,5], Jean-Pierre Barriot[3,4], Yajun Wu[1] and Guangli Wang[1]

[1] Shanghai Astronomical Observatory, Chinese Academy of Science, Shanghai 200030, People's Republic of China
[2] Applied Parallel Computing LLC, Lugano, Switzerland
[3] State Key Laboratory of Information Engineering in Surveying, Mapping and Remote Sensing, Wuhan University, Wuhan 430070, People's Republic of China
[4] University of French Polynesia, Geodesy Observatory of Tahiti, Laboratoire GEPASUD, BP 6570, 98702 Faaa airport, Tahiti, French

E-mail: jgyan@whu.edu.cn (Jianguo Yan)

Received 8 September 2019, revised 15 November 2019
Accepted for publication 19 November 2019
Published 15 January 2020

Abstract

This paper introduces a phase tracking method with a computational algorithm for planetary radio science implemented on NVIDIA GPUs. In contrast to the phase-locked loop phase counting method used in traditional Doppler data processing, this method fits the tracking data with optimal parameters into the shape expressed by Taylor expansion. The differential evolution (DE) algorithm is employed for polynomial fitting. In order to cope with the high computational intensity of the proposed phase tracking method, graphics processing units (GPUs) are employed. The method estimates the instantaneous phase, the frequency, the derivative of frequency (line-of-sight acceleration) and the total count phase for different integration scales. These observables can be further used in planetary radio sciences. The new method was tested on the Mars Express (MEX, ESA) and Chang'e 4 relay satellite (China) tracking data. In a real experiment with 400 K data block size and ∼80 000 DE solver objective function evaluations, we were able to achieve the target convergence threshold in 6.5 s, executing real-time processing on NVIDIA GTX580 and 2× NVIDIA K80 GPUs, respectively. The instantaneous Doppler precision for occultation research of this method is higher than the result of a traditional Doppler method. The precision of the integral Doppler (60 s integration) was 2 mrad s^{-1} and 4 mrad s^{-1} for MEX(3-way) and the Chang'e 4 relay satellite(3-way) respectively, which is equal to traditional Doppler results.

Keywords: phase tracking, Doppler dataprocessing, radiosciences, GPU, CUDA

(Some figures may appear in colour only in the online journal)

1. Introduction

In deep space exploration missions, radio measurements are often used to estimate the mass and gravity of planets, model their internal structure, and sound the media around planets. This type of research is generally called radio science [1]. The physical parameters of the electromagnetic signals that link the station and spacecraft change during its propagation due to the relative motion of the spacecraft and station, as well as from the influence of propagation media. Variations in the gravitational potential at the position of the spacecraft and station are also a factor. Physical parameters include phase, frequency, amplitude and polarization. The variation in these parameters can be used to estimate the atmospheric and ionospheric structure of planets [2–7], solar corona, planetary gravitational fields, shapes, mass [8–20], planetary rings [21–23] and ephemerides of planets [24–26]. Furthermore, parameter variation can verify the theory of general relativity, gravitational waves

[5] Author to whom any correspondence should be addressed.

detection and gravitational red shift [1, 27–30]. In planetary atmospheric and ionospheric structure studies, the parameters of interest are instantaneous amplitude, phase and frequency. For planetary gravity, ephemerides and the theory of general relativity, the parameters of interest are the integral Doppler or the total count phase. All these parameters can be retrieved through high-precision Doppler measurements.

Since the late 1960s, the Jet Propulsion Laboratory (JPL) has been conducting radio science experiments in early deep space explorations. Remarkable results have been achieved in the course of 50 years: the high-precision gravity field of the Moon and Mars have been determined by Doppler tracking [31–34]; the atmospheric components and ionospheric models of Mars and Venus have been studied from the radio science tracking data [7, 35, 36]; and the recent results about radio science from Cassini and Juno missions to Saturn and Jupiter [5, 18, 19, 26, 27, 37]. These achievements form a basis for further deep space explorations.

1.1. Planetary radio science hardware

The radio science research work conducted by JPL is supported by the deep space network (DSN) of NASA located at Goldstone (USA), Madrid (Spain) and Canberra (Australia). The DSN is equipped with 26, 34, and 70 m antennas and a Doppler tracking system [1]. The fifth generation of JPL Doppler processors was designed in the form of the so-called 'block series'. The block series are mainly used in precise orbit determination, planetary gravity recovery and general relativity research with a close-loop tracking model. The open-loop tracking model receivers were developed and applied in the space missions of the 1990s, such as the radio science receiver (RSR) by JPL [38] and the intermediate frequency modulation system (IFMS) by ESA [39]. The open-loop tracking model is used in atmospheric and ionospheric studies. Recently, some attempts have been made to apply the open-loop tracking model to planetary gravity research [40].

In Doppler data processing, the amount of computations is large and requires a high-performance computational device. The application specific integrated circuit (ASIC) technology is employed in the design of traditional Doppler extractors to compute the phase accumulation (also called phase counting) [41]. General-purpose computing devices also offer enough performance to be used in Doppler data processing software based on a GNU radio[6], e.g. the Universal Software Radio Peripheral (USRP). The USRP can process tracking data using FFT-based methods to realize aircraft signal tracking [42].

This paper introduces a new phase tracking method, which employs graphic processing units (GPUs) to compute phase, frequency and the frequency derivative of tracking data. The new algorithm fits the tracking data signal into the shape expressed by the Taylor polynomial with optimal phase and amplitude coefficients within every data block[7]. The method calculates the analytical form of phase expression in the neighborhood of the data block center and the amplitude with the slope of the signal. The amount of baseband fitting computations is large and is offloaded onto the GPUs. We show that real-time data processing can be achieved by using two NVIDIA Tesla K80 GPUs. The fitting is performed using the differential evolution (DE) algorithm [43] a well-known robust method for global optimization problems. From the analysis of the form of the phase, we further deduce the frequency, the derivative of frequency (line-of-sight acceleration) and the integral phase (total count phase) at different timescales [44]. These observables can be used in planetary radio science research to analyze planetary occultations and gravitational fields.

1.2. Differential evolution algorithm

Doppler data block fitting is a computationally expensive problem, as each objective function evaluation is a numerical integration of the time series. Fortunately, the integration can be easily parallelized. Moreover, an additional degree of parallelism is offered by certain kinds of optimization algorithms, such as DE.

The DE is a robust global optimization method widely used in various fields to solve multidimensional problems [45]. The DE algorithm originates from a genetic annealing algorithm first described by Price *et al* [46]. The DE algorithm won the International Contest on Evolutionary Optimization (ICEO) twice, in 1996 and 1997 [47, 48].

In DE, the initial population is randomly chosen within the parameter space, while the child parameters vectors are iteratively derived from their parents through a mutation procedure, depending on the objective function response (figure 1). The mutation is followed by the crossover path selection. In order to escape from local minima, DE introduces a weighting factor. The iterative process continues until the fulfilment of the convergence criteria.

1.3. GPGPU computing

The graphics processing unit (GPU) is a specialized processor originally designed specifically for accelerating video output with complex 3D scenes in games, CADs and visual effects. In order to optimize the speed of positioning and texturing of complex geometries that involve interpolation, the GPUs have become rich in floating-point throughput. Furthermore, the GPU architecture developed a massive parallelism as the fastest approach to process millions of independent triangles in 3D rendering. In the early 2000s, enthusiasts already turned their interest towards general-purpose computations on GPUs (GPGPU) for science and research. However, the GPU programming frameworks of that time, such as GLSL shading language, implied mandatory video output, did not offer some important features, such as fast-shared memory. The GPGPU market was revolutionized by the NVIDIA Corporation in 2007 with the release of the GeForce 8 consumer graphic cards. These cards support both traditional video processing and compute-only GPGPU pipelines. The GPGPU functionality has become widely available to users since the release of the CUDA v1.0 software development kit [49]. Also, NVIDIA

[6] www.gnuradio.org/.
[7] The data block is usually 2 s and sampling is 200 KHz.

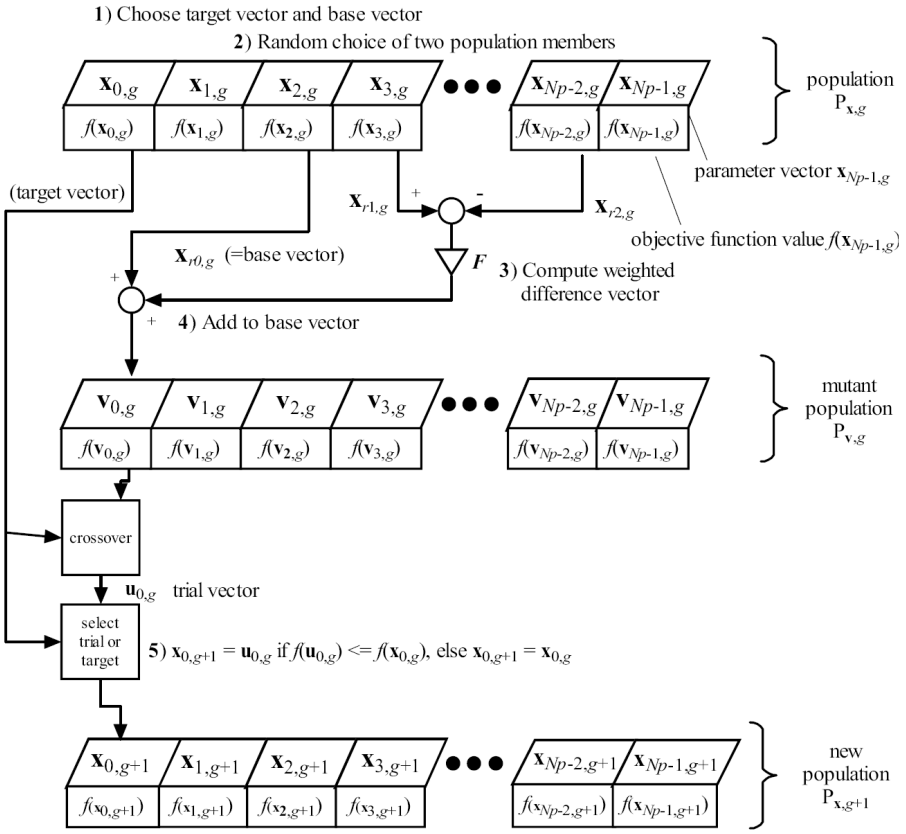

Figure 1. DE algorithm iteration flowchart.

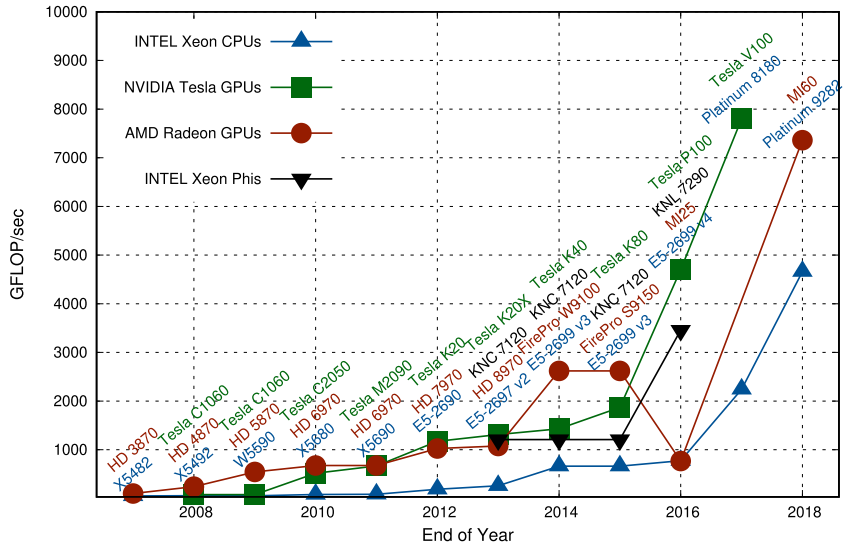

Figure 2. Comparison of double-precision (64 bits) computing performance.

released Tesla C870—the first compute-dedicated graphics card for data centers. Although early GPUs did not offer double-precision (64 bits) computation support, their single-precision (32 bits) performance was a lot higher than on CPUs of the same generation. For over a decade, NVIDIA GPU technology has experienced multiple architectural updates (Tesla, Fermi, Kepler, Maxwell, Volta). The latest NVIDIA Tesla V100 GPU has a double-precision peak throughput of 7.8 TFLOPS [50] (see figure 2). The CUDA toolkit and GPGPU ecosystem nowadays has grown into a large set of free de-facto standard libraries and frameworks for different purposes, such as linear algebra (CUBLAS, CUSPARSE), FFT (CUFFT), big data (Thrust), and machine learning (TensorFlow).

In our phase tracking method, the DE algorithm is employed for solving multidimensional optimization problems. The DE algorithm requires thousands of objective function evaluations, each integrates several hundred thousand points of time series. Along with the basic double precision floating-point multiply-add, the computation of objective function involves trigonometric operations. Since objective function integration

Table 1. PRSR data recording modes.

Output signal	Bandwidth/sampling	Quantization	Data rate (bit s^{-1})
Narrow band	16 KHz/32 KHz	8	256 000
		16	512 000
	25 KHz/50 KHz	8	400 000
		16	800 000
	50 KHz/100 KHz	8	800 000
		16	1600 000
	100 KHz/200 KHz	8	1600 000
		16	3200 000
Wide band	1 MHz/2 MHz	1,2,4,8	16 000 000
	2 MHz/4 MHz	1,2,4,8	32 000 000
	4 MHz/8 MHz	1,2,4	32 000 000
	8 MHz/16 MHz	1,2	32 000 000

is computationally expensive and parallelizable, the GPU processing becomes an ideal candidate. We offloaded this part to the GPU by using the Thrust C++ framework [51].

Table B1 compares the solution time cost on NVIDIA GTX 580 GPU and 2× Intel E5-2620v2 CPU, which have a peak double precision performance of 196 and 60 GFLOPs, respectively. Two implementations were evaluated on the CPU: OpenMP and Intel VML (Vector Math library). Our first version of a Doppler processing prototype is based on CPU OpenMP [52]. The GPU yielded a speedup of about 2× against a CPU for a small dataset below 2 Mbits. The speedup improved significantly for larger datasets and reached 9× for 256 Mbits. The OpenMP implementation however was faster than VML. Table B2 shows the GPU performance of a single objective function processing steps corresponding to equation (2) for a 1 Mbits dataset.

In our experiment, the data block size was 400 K (0.082 ms for one evaluation on GTX580) and is evaluated by the DE solver ∼80 000 times to reach the convergence threshold (totals 6.5 s on GTX580). Furthermore, by replacing GTX580 with 2× NVIDIA K80s (3.6 TFLOPs peak) we were able to achieve real-time processing.

2. Receiver and signal model

2.1. Receiver overview

The planetary radio science receiver (PSRS) started operation in 2008 and was developed under a contract between Shanghai Astronomical Observatory and the Southeast University of China. The design of PSRS is similar to the RSR receiver framework by JPL [38] with 70 MHz IF signal input. PSRS has two output channels: the first channel is a narrow band signal recorded on a hard drive after a two-stage down conversion from the IF signal; the second channel is a hardware Doppler output after a one-stage down conversion. Table 1 shows the available PRSR data recording modes. In addition to the PSRS receiver, we also developed a interface for the Chinese VLBI Data Acquisition System (CDAS) data acquisition device to process the Chang'e 4 relay satellite. The CDAS receiver was developed by the Shanghai Observatory to support the Change'e series VLBI tracking mission and records data with a VLBI Mark-V format standard. Details of performance parameters can be found in [53].

2.2. Signal model and objective function

The tracking data recorded on the hard disk had phase errors stemming from various physical origins. The continuous data stream was processed in segments or blocks of length T where the value of T is related to the motion of the spacecraft (the relation between length of T and motion of the spacecraft can be found in section 3.2.1), and is usually set to 2 s. If the relative timestamp in the center of the data block has the value zero, then the phase can be expanded by a finite Taylor polynomial within the interval $[-T/2, T/2]$:

$$\phi(t) = \phi(0) + \sum_{i=1}^{n} \frac{\phi^{(i)}(0)}{i!} t^i. \tag{1}$$

The value n is the order of Taylor expansion that is also related to the motion of the spacecraft. In most of the cases $n = 3$ meets the truncation error requirements when the block length is set to $T = 2$ s. Generally, the truncation error is set to the phase noise, a topic that will be discussed in section 3.2. The radio signal in the data block with the Taylor polynomial phase expression can be expressed as

$$\begin{aligned} s(t) &= (c_4 + c_5 t)\cos(\phi(t)) \\ &= (c_4 + c_5 t)\cos(c_0 + c_1 t + c_2 t^2 + c_3 t^3). \end{aligned} \tag{2}$$

Here, $c_{0\sim3}$ are the coefficients of Taylor polynomial:

$$\begin{aligned} c_0 &= \phi(0) \\ c_i &= \frac{\phi^i(0)}{i!}\Big|_{i=1,2,3}. \end{aligned} \tag{3}$$

The coefficients c_4 and c_5 are signal amplitude parameters. Moreover, c_5 is the slope of amplitude and it can be ignored when amplitude change is small with data length below 10 s.

The DE algorithm minimizes the objective function, which should be non-negative. From equation (2) we constructed two types of objective functions. The first one is the classical χ^2 function and the second one is based on the correlation function:

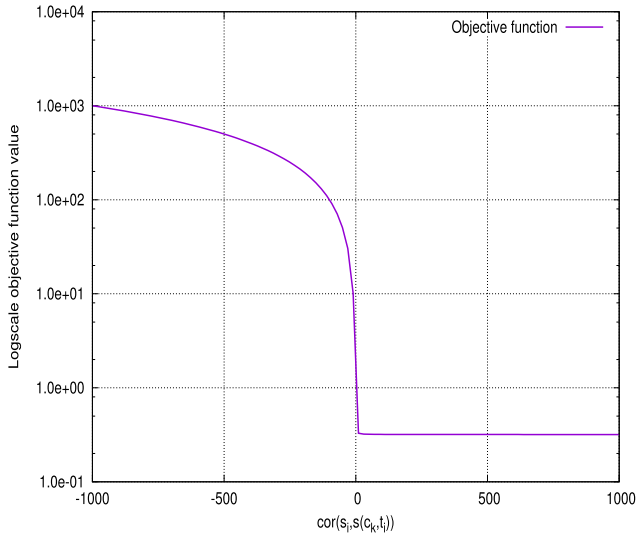

Figure 3. Relation between the objective function and the correlation coefficient.

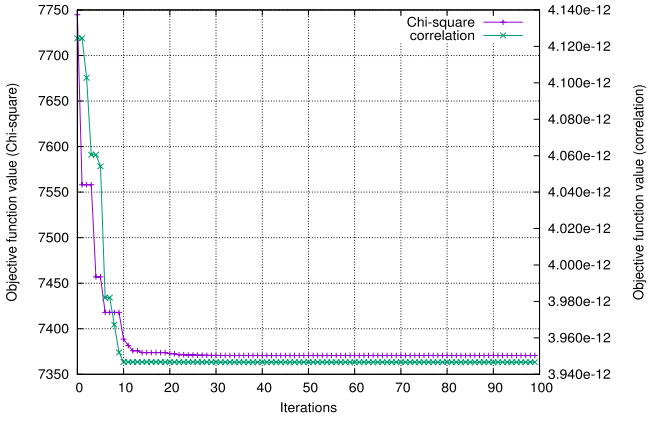

Figure 4. Comparison of convergence rate of two objective functions types (for the convenience of display, the correlation objective function value subtracted a constant of 0.318 309 8861).

$$F_{\text{obj}}^{\chi^2}(c_k) = \sum_{i=1}^{N} \frac{[s_i - s(c_k, t_i)]^2}{\sigma_i^2}\Big|_{\sigma_i=1} = \sum_{i=1}^{N} [s_i - s(c_k, t_i)]^2 \tag{4}$$

$$F_{\text{obj}}^{\text{cor}}(c_k) = \frac{1}{\arctan[\text{cor}(s_i, s(c_k, t_i))] + \frac{\pi}{2}}. \tag{5}$$

In equation (4), $\frac{1}{\sigma_i^2}$ is the weighting factor that is relative to the standard deviation of signal influenced by the physical environment. Influence is equal to every data point. So weighting factor can be set to 1. The $s(c_k, t_i)$ is the signal model constructed in equation (2), and s_i is the quantized signal value. The $F_{\text{obj}}^{\chi^2}(c_k)$ and $F_{\text{obj}}^{\text{cor}}(c_k)$ objective functions shall converge to the sum of noise power, and to $\frac{1}{\pi} \sim 0.318$, respectively. In equation (5) the signal model is slightly changed, such that the amplitude of signal is constant; otherwise, the objective function becomes divergent:

$$s(t) = A\cos(c_0 + c_1 t + c_2 t^2 + c_3 t^3). \tag{6}$$

The value A is the average amplitude of signal. Figure 3 shows the relation between $F_{\text{obj}}^{\text{cor}}(c_k)$ and $\text{cor}(s_i, s(c_k, t_i))$. Figure 3 also shows that the convergence is very fast when the correlation coefficient approaches zero. Figure 4 makes a comparison of the convergence rate of two objective functions types.

The data used for comparison is the real Mars express (MEX) tracking data with the baseband sampling of 200 KHz. Figure 4 shows that $F_{\text{obj}}^{\text{cor}}$ converges fast than $F_{\text{obj}}^{\chi^2}$ with 10 iterations. On the other hand, $F_{\text{obj}}^{\chi^2}$ requires 25 times iterations. Moreover, the computational difficulty of one $F_{\text{obj}}^{\text{cor}}$ evaluation is only 60% of the $F_{\text{obj}}^{\chi^2}$ function. In total, the $F_{\text{obj}}^{\text{cor}}$ takes 75% less time to compute a data block, as compared to $F_{\text{obj}}^{\chi^2}$. Although the $F_{\text{obj}}^{\text{cor}}$ is faster than $F_{\text{obj}}^{\chi^2}$, it cannot handle larger block sizes that have significant signal amplitude change.

Table 2. The DE algorithm control parameters.

Item	Meaning	Value
Dim_XC	Dimension of problem	6
XCmin[a]	The lower bound of parameters	*
XCman[a]	The upper bound of parameters	*
VTR	The expected fitness value of objective function	0
Itermax	The maximum number of iterations	200
F_XC	Mutation scaling factor	0.5
CR_XC	Crossover factor	0.85
Strategy	The strategy of the mutation operations	3|6

[a] Bound of parameters to be solved.

3. Data processing and error analysis

3.1. Data processing

This subsection will introduce the parameter setting for the DE algorithm, phase continuity checking and process flow in real data processing.

3.1.1. Determination of the range of parameters to be solved. A determination of the range of parameters to be solved is required when calling the DE algorithm, which must cover the true value of parameters. Because the DE algorithm is a kind of global optimization, generally speaking, a range of parameters can be defined, that cover the full range of variations of the parameters. However, this strategy will generate a huge amount of computations. Therefore, determining an initial value and *a priori* range of parameters is necessary for highly efficient computation. The range determination includes an initial range setting and running time range setting. Appendix A gives a discussion of these two kinds of

range settings based on the χ^2 function model mentioned in equation (4).

3.1.2. The DE algorithm control parameter setting. The DE algorithm runs under a set of control parameters. Table 2 explains these control parameters and values set.

There are six kinds of mutation operations strategies in the DE algorithm that affect the solution robustness and computation speed [45]. For a specific optimization problem, some tests are needed to determine the best mutation operations strategy. Two types of stop condition are generally used for parameters searching. The first one is by fixing the iteration times when a proper priori parameters range can be determined at running time. The second one is by setting the threshold of change of objective function or parameters. In practical applications, the parameters and objective function always remain the same after dozens of iterations because of the characteristics of the genetic algorithms. So, the first type of stop condition was used in our real data processing.

3.1.3. Phase continuity checking. A natural method to judge whether the solution converges is to check the continuity of instantaneous phase and frequency at the bound of two adjacent data blocks. Using equation (1) we can get the expression of phase and frequency:

$$\begin{aligned}\phi(t) =& c_0 + c_1 t + c_2 t^2 + c_3 t^3 \\ \mathrm{F}(t) =& \frac{\mathrm{d}\phi(t)}{\mathrm{d}t} \\ =& c_1 + 2c_2 t + 3c_3 t^2.\end{aligned} \tag{7}$$

Phase and frequency at the bound of two adjacent data blocks (n and $n+1$) are

$$\begin{aligned}\phi^n|_{\text{right}} &= c_0^n + c_1^n t + c_2^n t^2 + c_3^n t^3|_{t=T/2} \pmod{2\pi} \\ \phi^{n+1}|_{\text{left}} &= c_0^{n+1} + c_1^{n+1} t + c_2^{n+1} t^2 + \\ &\quad c_3^{n+1} t^3|_{t=-T/2} \pmod{2\pi} \\ \mathrm{F}^n|_{\text{right}} &= c_1^n + 2c_2^n t + 3c_3^n t^2|_{t=T/2} \\ \mathrm{F}^{n+1}|_{\text{left}} &= c_1^{n+1} + 2c_2^{n+1} t + 3c_3^{n+1} t^2|_{t=-T/2}.\end{aligned} \tag{8}$$

Checking whether the values of $\phi^n|_{\text{right}}$ and $\mathrm{F}^n|_{\text{right}}$ are equal to $\phi^{n+1}|_{\text{left}}$ and $\mathrm{F}^{n+1}|_{\text{left}}$ within the threshold of noise confirms the correctness of the parameter results from the DE algorithm. A real data processing example on MEX data shows the continuity of phase and frequency in appendix C. The noise of phase is about 50 mrad (1 σ, 1 s integration). The continuity of phase is therefore confirmed.

3.1.4. Data process flow. The software reads the initial parameters range and the DE algorithm controls parameters from the control file and runs automatically without manual intervention. Figure 5 gives the process flow. In radio measurement, some accidental factors exist that cause phase distortion and iterations divergence. In this situation, the software will automatically adjust parameter range and try to search again. The data block will be abandoned after three attempts.

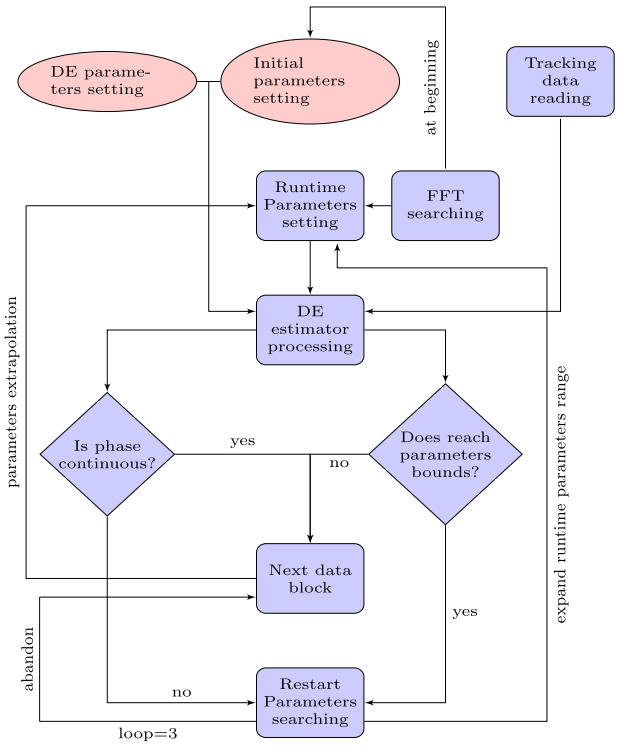

Figure 5. Data process flow.

3.2. Error analysis

There are three kinds of errors in data processing. The first error is the truncation error in phase calculation, which is also called the remainder of the Taylor expansion. The second error is linked to noise in the tracking data. The third is a system error caused by an equipment and propagation medium along the signal path. The remainder of the Taylor polynomial is relative to the block length and polynomial order. Random errors come from thermal noise of signal beacon, receivers and propagation medium along the signal path. System error can be eliminated by the construction of error models in high-level data processing, which is beyond the scope of this paper and will not be discussed.

3.2.1. Remainder of Taylor expansion. The remainder of Taylor polynomial has several forms of expression. A Lagrange error bound is usually used for error analysis. The Lagrange error bound of equation (1) can be written as

$$R_n(t) = \frac{\phi^{n+1}(\xi)}{(n+1)!} t^{n+1}\Big|_{\xi\in[0,t]} \tag{9}$$

ξ is a point within [0,t]. The max error within the data block is generally at the block border. The remainder at the block border is

$$\begin{aligned}R_n\left(\frac{T}{2}\right) &= \frac{1}{2^{n+1}(n+1)!}\phi^{(n+1)}(\xi)T^{n+1}\Big|_{\xi\in[0,\frac{T}{2}]} \\ &< \frac{1}{2^{n+1}(n+1)!}\left|\phi_{\max}^{(n+1)}\right|T^{n+1}.\end{aligned} \tag{10}$$

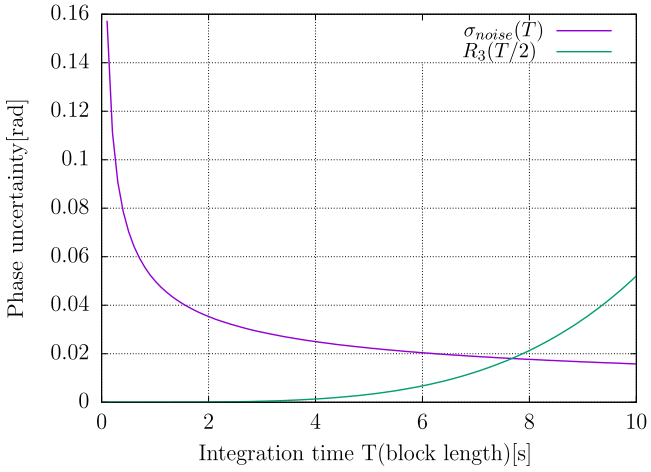

Figure 6. Variety of phase noise $\sigma_{\text{noise}}(T)$ and remainder $R_3(\frac{T}{2})$.

Here $\left|\phi_{\max}^{(n+1)}\right|$ is the maximum absolute value of the $n+1$th derivative of the phase within the data block. From equation (10) we can see that the upper bound of the remainder is relative to the order of the Taylor polynomial n, the length of data block T and the absolute value of maximum $n+1$th derivative of phase. Generally speaking[8], $n=3$ can ensure the remainder is small enough, with which the upper bound of $\left|\phi_{\max}^{(n+1)}\right|$ will be 3×10^{-7} rad s^{-4} (see appendix D). When the block length is not so long (less than 10 s), the upper bound of the truncation error of the Taylor polynomial is 10^{-5} rad. But in some special cases, such as spacecraft passing across a perigee or flying-by, a giant planet amplitude of $\left|\phi_{\max}^{(n+1)}\right||_{n=3}$ cannot be ignored (this term is about 2×10^{-3} rad s^{-4} while MEX passes across a perigee) and $n=3$ is not enough for high precision data processing. In this situation $n=4$ will be worked and the upper bound of truncation error could be controlled within 10^{-4} rad. Derivatives of phase can be estimated from the derivatives of line-of-sight velocity using a forecast orbit:

$$\begin{aligned}\left|\phi_{\max}^{(n+1)}\right| &\simeq \frac{2\pi f_0}{c}\left|v_{\max}^{(n)}\right| \qquad \text{(1-way)}\\ \left|\phi_{\max}^{(n+1)}\right| &\simeq \frac{4\pi M_2 f_0}{c}\left|v_{\max}^{(n)}\right| \qquad \text{(3-way)}.\end{aligned} \tag{11}$$

In theory, if there is no effect of thermal noise, the truncation error can be adjusted to be very small by tuning the parameters n and T. Nevertheless the thermal noise cannot be eliminated. To excessively reduce the truncation error is a futile effort. So the threshold of truncation error can be set to the thermal noise of phase $\sigma_{\text{noise}}(T)$. Here T is the integration span for measuring phase noise that is exactly the block length. Pätzold *et al* have given a relative expression of $\sigma_{\text{noise}}(T)$:

$$\sigma_{\text{noise}}(T) = \sigma_{\text{noise}}(1)\sqrt{\frac{1}{T}} \tag{12}$$

$\sigma_{\text{noise}}(1)$ is the standard thermal noise with an integration span of 1 s. From the equation (12) we can infer that thermal noise can be effectively suppressed by increasing the integration time.

A choice of T to balance the truncation error and thermal noise from equations (10) and (12) exists. The truncation error and T are positively correlated. The thermal noise and T are negatively correlated. The optimal length of T can be found by balancing the computation amount and the data process precision. Figure 6 gives the relationship of the truncation error and phase thermal noise relative to block length in the MEX tracking case ($\sigma_{\text{noise}}(1)=50$ mrad). From figure 6 we can see that the truncation error will be less than phase thermal noise when the block length is shorter than 7 s. In actual data processing, to ensure that the truncation error is less than the phase noise and improve the data processing efficiency, the data block length is generally set to 2 s.

Precision evaluation of the Doppler could be made from measurement noise, which is generally relative to integral span. Different integral spans are selected in different research in radio science. In planetary occultation research integral span is often set below 1 s to get high measurement resolution. In gravity field research, the integral span is set to dozens of seconds to ensure precision and gravity field resolution. While in general relative experiment integral span is equal to 10^4 s to achieve extreme Doppler precision. The relationship between integral span and Doppler precision is given by equation (12).

3.2.2. Random phase noise. Random error noise in data will affect the estimation of phase and it can be used as criteria for truncation error as described above. Random noise comes from two sources. The first source is the thermal noise that might come from the signal source, the onboard transponder, and the station receiver. The second is random interference of solar phase scintillations along the signal path. Carrier phase error variance can be expressed as [38]

$$\begin{aligned}\sigma^2_{\text{noise}}|_{\text{1-way}} &= \sigma_S^2 + \frac{1}{\rho_L}\\ \sigma^2_{\text{noise}}|_{\text{3-way}} &= \frac{M^2(B_{TR}-B_L)}{P_C/N_0|_{U/L}} + \sigma_S^2 + \frac{1}{\rho_L}.\end{aligned} \tag{13}$$

Here,

- σ_S^2 is the contribution to carrier loop phase error variance due to solar phase scintillations;
- ρ_L is the downlink carrier loop signal-to-noise ratio;
- M is the transponder ratio;
- B_{TR} is the one-sided, noise-equivalent, transponder carrier loop bandwidth;
- B_L is the one-sided, noise-equivalent, loop bandwidth of downlink carrier loop; and
- $P_C/N_0|_{U/L}$ is the uplink carrier power-to-noise spectral density ratio.

Phase error variance contributed by solar phase scintillations is related to the angle SEP (Sun Earth Probe). This effect is greater when the sun is near the direction of observation. Equation (14) gives the relation between σ_S^2 and SEP [38]:

$$\sigma_S^2 = \frac{C_{\text{band}}C_{\text{loop}}}{(\sin\theta_{\text{SEP}})^{2.45}B_L^{1.65}}\Big|_{\theta_{\text{SEP}}\in[5^\circ,27^\circ]}. \tag{14}$$

[8] In the following contents of this paper, if not specified, the default value of $n=3$.

In equation (14) $C_{\text{band}}, C_{\text{loop}}$ are constants that vary with frequency band. For X band of up and down link $C_{\text{band}} = 1.9 \times 10^{-6}, C_{\text{loop}} = 5.9$. A new and more complex piecewise functions model is given by [54], which will be considered in our future experiments.

The typical magnitudes of phase noise for two-/three-way tracking at X band are [55]

$$\sigma^2_{\text{noise}} \leqslant \begin{cases} 0.1 \text{ rad} & \text{residual carrier} \\ 0.02 \text{ rad} & \text{suppressed carrier BPSK} \\ 0.005 \text{ rad} & \text{QPSK.} \end{cases} \quad (15)$$

Equation (15) gives the upper bound of phase noise variance for three types of carrier modulation.

4. Applications

We can form several kinds of observables by using the Taylor polynomial coefficients result from the DE algorithm. These include integration Doppler, instantaneous Doppler, the total count phase and line-of-sight acceleration.

4.1. Doppler observables

4.1.1. Integration Doppler. The integration Doppler is an important observation type in planetary gravity research. The original definition of the integration Doppler is the phase change during a fixed count interval [44]:

$$F_{\text{int\_dop}} = \frac{\phi_{t_e} - \phi_{t_s}}{T_c}. \quad (16)$$

Here we ignore the frequency bias for the convenience of discussion. t_e is the station time at the end of count interval and t_s is the station time at the beginning of the count interval. T_c is the count interval length that varies for different research objects. Typical count times have durations of tens of seconds in planetary gravity research while spacecrafts are orbiting a planet. In testing the theory of general relativity and gravitational wave searches the counting interval will be a few thousand seconds for extremely high Doppler measurement precision during an interplanetary cruise [1, 27, 28, 30].

The typical data block length is 2 s and the limitation of data block length is 20 s, which is limited by the processing ability of the GPUs. We can use the phase connection to form longer integration Doppler observables:

$$\begin{aligned} \Phi_{\text{total}} &= \sum_{i=1}^{N} \left[\phi_i\left(\frac{T}{2}\right) - \phi_i\left(-\frac{T}{2}\right)\right]\Big|_{N=\frac{T_c}{T}} \\ F_{\text{int\_dop}} &= \frac{\Phi_{\text{total}}}{T_c}. \end{aligned} \quad (17)$$

In equation (17) i is the serial number of the block, $\phi_i(\frac{T}{2})$ can be evaluated by phase expression (equation (7)), Φ_{total} is the phase change within count interval T_c, which is also a new kind of observation type in planetary science research [44]. Column 8 of appendix C gives the example of $[\phi_i(\frac{T}{2}) - \phi_i(-\frac{T}{2})]$. Uncertainty of the integration Doppler can be expressed as:

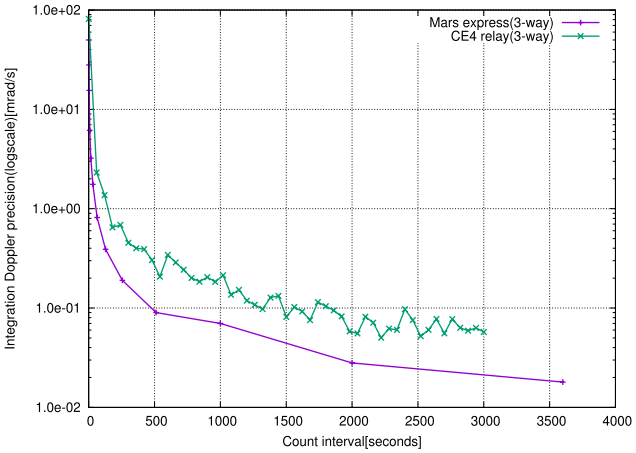

Figure 7. Precision of integration Doppler changes with count interval.

$$\sigma^2_{\text{int\_dop}} = \frac{\sigma^2(T)}{NT}. \quad (18)$$

The meaning of equation (18) is the same as equation (12). $\sigma^2(T)$ is the phase variance of the block or the phase discontinuous variance at the block border.

Figure 7 shows the precision of the integration Doppler with different interval scales in the MEX and CE4 data process. The Doppler precision is about 50 mrad s^{-1} for MEX and 80 mrad s^{-1} for the CE4 relay satellite with one second integration span. The precision of the integral Doppler resulting from our fitting method has the same level with traditional the PLL method [56].

4.1.2. Instantaneous Doppler. The instantaneous Doppler is used in planetary occultations research in which high Doppler resolution is required at the ingress or egress of radio signals into or out of planetary atmospheres. There are two kinds of approximate approaches to compute an instantaneous Doppler. The first is to decrease the count interval [44] and use the integration Doppler to approximate the instantaneous Doppler. The second is using short-time fast Fourier transform (FFT) to compute an average frequency of a short data block [56]. The Doppler precision of these two approaches will obey equation (12), that is 3.16 times of $\sigma_{\text{noise}}(1)$ when the Doppler sampling rate is 10 Hz.

Using equation (7) we can conveniently calculate the instantaneous Doppler at any time tag within the data block and the precision is guaranteed by the truncated error $\sigma_{\text{noise}}(2)$, which is 0.7 times of $\sigma_{\text{noise}}(1)$. Thus, the instantaneous Doppler calculated from Taylor polynomial has higher precision than the method of the short count interval or method of short-time FFT.

As an example, For the Venus Express (VEX) one-way open-loop radio occultation experiments we processed the tracking data (doy 343) [57] and compared our result[9](1 s integration span and 10 Hz output[10]) with the 10 Hz output

[9] Shanghai Observatory of China, SHAO.
[10] Evaluation of Taylor polynomia at every point.

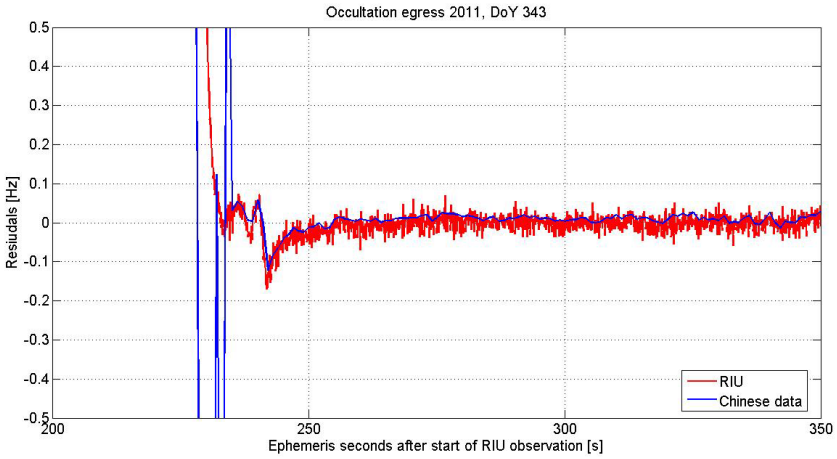

Figure 8. VEX occultation result comparison of SHAO and RIU.

result from Rheinisches Institut für Umweltforschung (RIU) by using the FFT method. Figure 8 shows the comparison. From figure 8 we can see our result has lower noise than the computed result by RIU.

4.2. Line-of-sight acceleration observables

From equation (11) we can see that derivatives of phase are related to the derivatives of line-of-sight velocity that the second derivative of phase can be approximated as a function of line-of-sight acceleration:

$$\phi^{(2)} \simeq \frac{2\pi f_0}{c} a_{\rm los} \quad \text{(1-way)}$$
$$\phi^{(2)} \simeq \frac{4\pi M_2 f_0}{c} a_{\rm los} \quad \text{(3-way)}. \tag{19}$$

A strict and full expansion of equation (19) can be found in appendix E, which gives the connection between the observable of $\phi^{(2)}$ and the dynamic state of the spacecraft and stations. In a MEX tracking case, the first-order $(1/c)$ approximates to 10^{-3} m s^{-1} and the second-order $(1/c^2)$ approximates to 10^{-4} m s^{-1}.

Based on the concept of appendix E we gave an estimation of the mass and second-order coefficients of gravity of Phobos [58]. The line-of-sight acceleration observable ($\phi^{(2)}$) directly reflects the kinematic state of the spacecraft ($\mathbf{r}_2, \dot{\mathbf{r}}_2, \ddot{\mathbf{r}}_2$) and can be used to estimate the dynamic parameters relative to spacecraft ($\ddot{\mathbf{r}}_2$) by employing a reference orbit. It also can be used in a least square regression combined with traditional Doppler observables to solve parameters like gravity field coefficients.

5. Conclusion

This paper introduces a new phase tracking method for planetary radio science research based on general purpose computing on GPU (GPGPU) technology. The proposed method gives the same precision in integration Doppler processing as the traditional PLL phase counting method (50 mrad s^{-1} for 1 s and 2 mrad s^{-1} for 60 s integration span in the case of MEX data). This method has three main advantages over existing hardware and software Doppler processing solutions. Firstly, through the adjustment of the polynomial order and data block length, the analytical form of phase (frequency) will give higher precision for the instantaneous Doppler required in planetary occultation research (10 Hz or 100 Hz sampling rate). Secondly, the method can give the line-of-sight acceleration observable, which directly reflects the dynamic state of the spacecraft (see appendix E).Using line-of-sight acceleration we can directly solve the dynamic parameters with respect to a reference orbit. Thirdly, GPUs are less expensive and easier for software development, compared to the traditional ASIC-based PLL Doppler processing equipment.

Acknowledgments

We appreciate constructive comments from two anonymous reviewers and the editor that improved the manuscript significantly. This work has been supported by the National Natural Science Foundation of China, the Astronomical Joint Program (Grant Nos. U1531136, U1831132) and the DAR Grant in planetology from the French Space Agency (CNES). We thank Mr Gou Wei from the Sheshan 25 meter Observatory for his assistance in MEX tracking, Prof Meng Qiao, Chen Congyan and Lu Rongjun of Southeast University of China for advice on Doppler data processing, and Prof. Ping Jinsong of the National Observatory of China for helpful conversations. We thank Professor Martin Päetzold for providing us with the VEX occultation result in figure 8.

Appendix A. *A priori* parameter range setting

The determination of the proper initial range of parameters needs an estimation of parameters. From equation (3) we can see that the polynomial coefficients are determined by derivatives of phase at the block center. So if we can estimate the derivatives of phase at the block center then the polynomial coefficients can be determined properly. The detailed estimation process is as follows.

1. c_0 is the instantaneous phase at the block center and the range can be set as $[0, 2\pi]$.
2. c_1 is the instantaneous frequency at the block center (rad s^{-1}). It can be determined through FFT computation of a small piece of data extracted from the block center. The range of c_1 can be set as $\pm 10\%$ of c_1.
3. c_2 is equal to half of the second derivative of phase at the block center. So the value of c_2 can be estimated by the central difference method through three equally spaced frequency values near the block center. The frequency value is calculated as step 2.
4. c_3 is the 1/6 of third derivative of phase at the block center. This term is very small and will not be greater than 10 in all situations. In real data processing, the initial range of c_3 is set to $[-50, 50]$ for the sake of insurance.
5. c_4 is the amplitude of signal. It can be determined by the FFT algorithm done at step 2. The range of c_4 can be set as $\pm 10\%$ of c_4.
6. c_5 is the slope of amplitude, where relative uncertainty is big when block length is not long enough. For the sake of insurance its range is set as $[-0.2c_4\frac{1}{T}, 0.2c_4\frac{1}{T}]$.

If there is a forecast orbit of spacecraft derivatives of phase at the block center, this also can be properly estimated from orbit using equation (11).

Determination of the range of parameters at running time is exactly the automatic tracking of the signal. Extrapolation is used in coefficients of Taylor polynomial estimation from the nth block to the $n+1$th block. The specific estimation of the running time range is as follows.

1. Range of c_0^{n+1} is the same as initial range setting $[0, 2\pi]$
2. Value of c_1^{n+1} can be extrapolated from the first-order phase derivative of block n (equation (1)): $\dot{\phi}^n(t) = c_1^n + 2c_2^n t + 3c_3^n t^2$. So the value is $c_1^{n+1} = \dot{\phi}^n(T)$, and range could be set as $[\dot{\phi}^n(T/2), \dot{\phi}^n(3T/2)]$[11].
3. Value of c_2^{n+1} can be extrapolated as c_1^{n+1}, which is $c_2^{n+1} = 0.5\ddot{\phi}^n(T)$. Range could be set as $[0.5\ddot{\phi}^n(T/2), 0.5\ddot{\phi}^n(3T/2)]$.
4. Value of c_3 is small and the range can be further narrowed from the result of the first time of DE calling.
5. Range of c_4^{n+1} is $[c_4^n - 0.1c_4^n, c_4^n + 0.1c_4^n]$.
6. Range of c_5 can be fixed as c_3.

Range settings by means of extrapolation of c_1^{n+1} and c_2^{n+1} are effective in most situations when derivatives of phase are monotonic functions. Nevertheless, when derivatives of phase are not monotonic functions within two blocks the range of parameters will not cover the true value, then the parameter search will fail. This generally happens while the spacecraft crosses the orbital apogee or perigee. The software will automatically restart a search after properly enlarging the range of parameters. Meanwhile the values of c_3 and c_5 are the random distribution when data length is not long enough (that is the signal-to- noise ratio is not big enough) (appendix C).

Appendix B. Tables about GPU performance

Table B1. CPU and GPU computing speed comparison.

Data volume (Mbits)	GTX580 (GPU) (ms)	OpenMP (CPU) (ms)	VML (CPU) (ms)
1	0.2	0.5	0.7
2	0.3	0.6	1.6
4	0.3	2.2	3.5
8	0.5	6.5	7.8
16	0.9	13.4	13.3
32	1.7	25.2	25.2
64	3.3	48.6	50.2
128	6.4	68.6	100.7
256	12.6	107.3	201.2

Table B2. Single objective function processing steps on NVIDIA GTX580 (1 Mbit dataset).

Manipulation	Time consumed (ms)
Array initialization	0.039
Elements square of array	0.015
Array linear algebra operation	0.017
Array trigonometric operation	0.016
Array summation	0.118
Total time[a]	0.205

[a] Without host↔GPU data transfer time.

[11] The sign will be decided by software automatically.

Appendix C. Phase tracking output example for MEX tracking

		UTC time	c_0(rad)	c_1(rad/s)	c_2(rad/s^2)	c_3	c_4	c_5	total_phase	RSS	data quality index
	(border)	2013-12-28T19:24:38	6.102	146782.529							
block1	(center)	2013-12-28T19:24:39	5.670	146566.029	-108.151807	0.066	4728.3	6.7	293132.189	3424636.172	1
	(border)	2013-12-28T19:24:40	2.563	146349.922							
	(border)	2013-12-28T19:24:40	2.585	146349.721							
block2	(center)	2013-12-28T19:24:41	3.319	146133.984	-107.928933	-0.040	4713.0	-18.4	292267.887	3417344.713	1
	(border)	2013-12-28T19:24:42	1.824	145918.005							
	(border)	2013-12-28T19:24:42	1.831	145918.155							
block3	(center)	2013-12-28T19:24:43	4.412	145702.273	-107.838436	0.068	4721.2	-10.5	291404.683	3425031.927	1
	(border)	2013-12-28T19:24:44	4.946	145486.801							
		2013-12-28T19:24:44	4.933	145486.642							
...		2013-12-28T19:24:45	3.474	145271.151	-107.703009	0.028	4749.4	-2.9	290542.359	3427429.823	1
		2013-12-28T19:24:46	0.237	145055.830							
		2013-12-28T19:24:46	0.238	145055.809							
...		2013-12-28T19:24:47	1.568	144840.493	-107.600678	0.038	4710.2	2.9	289681.063	3423038.571	1
		2013-12-28T19:24:48	1.325	144625.406							
		2013-12-28T19:24:48	1.316	144625.163							
		2013-12-28T19:24:49	5.865	144410.414	-107.439969	-0.044	4725.1	-35.5	288820.741	3419870.188	1
		2013-12-28T19:24:50	2.878	144195.403							
		2013-12-28T19:24:50	2.893	144195.292							
		2013-12-28T19:24:51	4.936	143980.762	-107.331095	-0.044	4726.0	-0.9	287961.436	3424449.594	1
		2013-12-28T19:24:52	5.946	143765.968							
		2013-12-28T19:24:52	5.962	143766.015							
		2013-12-28T19:24:53	5.951	143551.478	-107.244130	0.016	4711.1	-4.7	287102.989	3424489.034	1
		2013-12-28T19:24:54	5.081	143337.038							
		2013-12-28T19:24:54	5.106	143337.164							
		2013-12-28T19:24:55	3.608	143122.853	-107.113158	0.028	4710.5	-5.7	286245.762	3419445.809	1
		2013-12-28T19:24:56	1.512	142908.711							
		2013-12-28T19:24:56	1.497	142908.715							
		2013-12-28T19:24:57	5.237	142694.705	-106.952688	0.035	4709.9	2.9	285389.480	3418848.526	1
		2013-12-28T19:24:58	2.417	142480.904							
		2013-12-28T19:24:58	2.437	142480.624							
		2013-12-28T19:24:59	5.570	142267.018	-106.825240	-0.015	4682.0	6.7	284534.007	3433902.863	1
		2013-12-28T19:25:00	2.398	142053.323							
...											
...											

Here, the integration length of total_phase (colum 8 above) is the block length

Table D1. Related parameters of the error remainder estimation of MEX and Cassini.

Arcs/band	σ_{noise} (mrad)[c]	Polynomia order	Block length (s)	$\lvert\phi^{(2)}_{\max}\rvert$ (rad s^{-2})	$\lvert\phi^{(3)}_{\max}\rvert$ (rad s^{-3})	$\lvert\phi^{(4)}_{\max}\rvert$ (rad s^{-4})	$\lvert\phi^{(5)}_{\max}\rvert$ (rad s^{-5})
				$\lvert a_{\max}\rvert$ (m s^{-2})	$\lvert a^{(1)}_{\max}\rvert$ (m s^{-3})	$\lvert a^{(2)}_{\max}\rvert$ (m s^{-4})	$\lvert a^{(3)}_{\max}\rvert$ (m s^{-5})
Mex(cruise)/X(2AU) [a]	50	2	10	7×10^{0}	5×10^{-4}	3×10^{-7}	
				3×10^{-2}[e]	1×10^{-6}	1×10^{-10}	
Mex(orbiting)/X	50	4|3[d]	2	8×10^{2}	6×10^{-1}	2×10^{-3}	3×10^{-6}
				2×10^{0}	2×10^{-3}	6×10^{-6}	8×10^{-9}
Cas(cruise)/X(10AU)[b]	20	2	10	7×10^{0}	5×10^{-4}	3×10^{-7}	
				3×10^{-2}[e]	1×10^{-6}	1×10^{-10}	
Cas(orbiting)/X[b]	20	4|3[d]	2	3×10^{3}	2×10^{0}	3×10^{-3}	6×10^{-6}
				8×10^{0}	6×10^{-3}	8×10^{-6}	2×10^{-8}

[a] Three-way tracking.
[b] Three-way tracking.
[c] One second integration time.
[d] Four order when near perigee, three order with normal arcs.
[e] The main contribution is the rotation of the earth.

Appendix D. Remainder estimation of MEX and Cassini

Taylor series remainder estimations for MEX and Cassini tracking.

Appendix E. Observation function of second derivative of phase

Acronyms:

- 1 foot mark means uplink station
- 2 foot mark means satellite
- 3 foot mark means downlink station
- c speed of light in vacuum
- t_i coordinate time at position i
- $\mathbf{r}_i$ position vector of object i in inertia frame
- $\mathbf{r}_{ij}$ position vector of object j relative to i
- $\dot{\mathbf{r}}_i$ velocity vector of object i in inertia frame
- $\dot{\mathbf{r}}_{ij}$ velocity vector of object j to i
- $\ddot{\mathbf{r}}_i$ acceleration vector of object i in inertia frame
- F_T frequency transmitted from uplink station
- M_2 transponder turnaround ratio onboard
- F_R frequency received by downlink station
- τ_3 atomic clock of downlink station
- r_{ij} distance from position i to j
- $\dot{r}_{ij}$ deviation of distance from position i to j
- Φ_i Newtown gravitation at position i
- $\dot{s}_i$ velocity magnitude of object i relative to Sun
- SSB Solar System Barycenter
- $L_B = 1.550\,520^{-8}$ Lagrangian constant of astronomy.

E.1. Two-/three-way tracking model

Moyer gives a precise formula accurate to $1/c^2$ describing the sky frequency received by the downlink station in two-/three-way tracking models [59].

$$(1-\frac{F_R}{M_2F_T}) = \frac{1}{c}(\dot{r}_{12}+\dot{r}_{23}) + \frac{1}{c^2}\left[\dot{r}_{12}\dot{p}_{12}+\dot{r}_{23}\dot{p}_{23} - \dot{r}_{12}\dot{r}_{23} + (\phi_1-\phi_3) + \frac{1}{2}(\dot{s}_1^2-\dot{s}_3^2)\right]. \tag{E.1}$$

Using above equation, the derivative of F_R to τ_3 can be written as($1/c$ terms):

$$\frac{\mathrm{d}F_R}{\mathrm{d}\tau_3}\Big|_{o(1/c)} = -\frac{M_2F_T}{c}\left(\frac{\mathrm{d}\dot{r}_{12}}{\mathrm{d}\tau_3}+\frac{\mathrm{d}\dot{r}_{23}}{\mathrm{d}\tau_3}\right). \tag{E.2}$$

Expansion of the right side of the above equation:

$$\begin{aligned}\frac{\mathrm{d}\dot{r}_{12}}{\mathrm{d}\tau_3} &= \frac{\partial\dot{r}_{12}}{\partial t_1}\frac{\mathrm{d}t_1}{\mathrm{d}t_2}\frac{\mathrm{d}t_2}{\mathrm{d}t_3}\frac{\mathrm{d}t_3}{\mathrm{d}\tau_3} + \frac{\partial\dot{r}_{12}}{\partial t_2}\frac{\mathrm{d}t_2}{\mathrm{d}t_3}\frac{\mathrm{d}t_3}{\mathrm{d}\tau_3}\\ \frac{\mathrm{d}\dot{r}_{23}}{\mathrm{d}\tau_3} &= \frac{\partial\dot{r}_{23}}{\partial t_2}\frac{\mathrm{d}t_2}{\mathrm{d}t_3}\frac{\mathrm{d}t_3}{\mathrm{d}\tau_3} + \frac{\partial\dot{r}_{23}}{\partial t_3}\frac{\mathrm{d}t_3}{\mathrm{d}\tau_3}.\end{aligned} \tag{E.3}$$

Expansion of partial derivatives of velocity to coordinate time:

$$\begin{aligned}\frac{\partial\dot{r}_{12}}{\partial t_1} &= +\frac{1}{r_{12}^3}(\mathbf{r}_{12}\cdot\dot{\mathbf{r}}_1)(\mathbf{r}_{12}\cdot\dot{\mathbf{r}}_{12}) - \frac{1}{r_{12}}(\dot{\mathbf{r}}_1\cdot\dot{\mathbf{r}}_{12}+\mathbf{r}_{12}\cdot\ddot{\mathbf{r}}_1)\\ \frac{\partial\dot{r}_{12}}{\partial t_2} &= -\frac{1}{r_{12}^3}(\mathbf{r}_{12}\cdot\dot{\mathbf{r}}_2)(\mathbf{r}_{12}\cdot\dot{\mathbf{r}}_{12}) + \frac{1}{r_{12}}(\dot{\mathbf{r}}_2\cdot\dot{\mathbf{r}}_{12}+\mathbf{r}_{12}\cdot\ddot{\mathbf{r}}_2)\\ \frac{\partial\dot{r}_{23}}{\partial t_2} &= +\frac{1}{r_{23}^3}(\mathbf{r}_{23}\cdot\dot{\mathbf{r}}_2)(\mathbf{r}_{23}\cdot\dot{\mathbf{r}}_{23}) - \frac{1}{r_{23}}(\dot{\mathbf{r}}_2\cdot\dot{\mathbf{r}}_{23}+\mathbf{r}_{23}\cdot\ddot{\mathbf{r}}_2)\\ \frac{\partial\dot{r}_{23}}{\partial t_3} &= -\frac{1}{r_{23}^3}(\mathbf{r}_{23}\cdot\dot{\mathbf{r}}_3)(\mathbf{r}_{23}\cdot\dot{\mathbf{r}}_{23}) + \frac{1}{r_{23}}(\dot{\mathbf{r}}_3\cdot\dot{\mathbf{r}}_{23}+\mathbf{r}_{23}\cdot\ddot{\mathbf{r}}_3).\end{aligned} \tag{E.4}$$

The relation between coordinate time and station time [59]:

$$\frac{\mathrm{d}t_3}{\mathrm{d}\tau_3} = (1-L_B)\left(1-\frac{2\Phi_3}{c^2}-\frac{\dot{s_3}^2}{c^2}\right)^{-\frac{1}{2}} \approx 1+\frac{\Phi_3}{c^2}+\frac{\dot{s_3}^2}{2c^2}-L_B. \tag{E.5}$$

The relation of coordinate time of different objects and definitions of relative velocity:

$$\begin{aligned}
\frac{\mathrm{d}t_1}{\mathrm{d}t_2} &= 1 - \frac{\dot{r}_{12}}{c} - \frac{\dot{r}_{12}\dot{p}_{12}}{c^2} \\
\frac{\mathrm{d}t_2}{\mathrm{d}t_3} &= 1 - \frac{\dot{r}_{23}}{c} - \frac{\dot{r}_{23}\dot{p}_{23}}{c^2} \\
\frac{\mathrm{d}t_1}{\mathrm{d}t_2}\frac{\mathrm{d}t_2}{\mathrm{d}t_3} &= 1 - \frac{\dot{r}_{12}+\dot{r}_{23}}{c} + \frac{\dot{r}_{12}\dot{r}_{23} - \dot{r}_{12}\dot{p}_{12} - \dot{r}_{23}\dot{p}_{23}}{c^2} \\
\dot{r}_{12} &= \frac{\mathbf{r}_{12}}{r_{12}} \cdot \dot{\mathbf{r}}_{12} \\
\dot{r}_{23} &= \frac{\mathbf{r}_{23}}{r_{23}} \cdot \dot{\mathbf{r}}_{23} \\
\dot{p}_{12} &= \frac{\mathbf{r}_{12}}{r_{12}} \cdot \dot{\mathbf{r}}_{1} \\
\dot{p}_{23} &= \frac{\mathbf{r}_{23}}{r_{23}} \cdot \dot{\mathbf{r}}_{2} \\
\dot{\mathbf{r}}_{12} &= \dot{\mathbf{r}}_2 - \dot{\mathbf{r}}_1 \\
\dot{\mathbf{r}}_{23} &= \dot{\mathbf{r}}_3 - \dot{\mathbf{r}}_2.
\end{aligned} \tag{E.6}$$

By substituting equations (E.2)–(E.6) into (E.1) we can get the first order of $1/c$ expansion for the derivative of F_R to τ_3.

The expansion of $1/c^2$ terms of equation (E.1)[12]:

$$\begin{aligned}
\frac{\mathrm{d}F_R}{\mathrm{d}\tau_3}\Big|_{o(1/c^2)} &= -\frac{M_2 F_T}{c^2}\left[\frac{\mathrm{d}(\dot{r}_{12}\dot{p}_{12})}{\mathrm{d}\tau_3} + \frac{\mathrm{d}(\dot{r}_{23}\dot{p}_{23})}{\mathrm{d}\tau_3} - \frac{\mathrm{d}(\dot{r}_{12}\dot{r}_{23})}{\mathrm{d}\tau_3}\right] \\
&= -\frac{M_2 F_T}{c^2}\left[\frac{\partial \dot{r}_{12}}{\partial \tau_3}\dot{p}_{12} + \frac{\partial \dot{p}_{12}}{\partial \tau_3}\dot{r}_{12}\right. \\
&\quad \left. + \frac{\partial \dot{r}_{23}}{\partial \tau_3}\dot{p}_{23} + \frac{\partial \dot{p}_{23}}{\partial \tau_3}\dot{r}_{23} - \frac{\partial \dot{r}_{12}}{\partial \tau_3}\dot{r}_{23} - \frac{\partial \dot{r}_{23}}{\partial \tau_3}\dot{r}_{12}\right].
\end{aligned} \tag{E.7}$$

Some terms have been expanded in equations (E.3) and (E.6) and the remains can be expanded as

$$\begin{aligned}
\frac{\partial \dot{p}_{12}}{\partial \tau_3} &= \frac{\partial \dot{p}_{12}}{\partial t_1}\frac{\mathrm{d}t_1}{\mathrm{d}t_2}\frac{\mathrm{d}t_2}{\mathrm{d}t_3}\frac{\mathrm{d}t_3}{\mathrm{d}\tau_3} + \frac{\partial \dot{p}_{12}}{\partial t_2}\frac{\mathrm{d}t_2}{\mathrm{d}t_3}\frac{\mathrm{d}t_3}{\mathrm{d}\tau_3} \\
\frac{\partial \dot{p}_{23}}{\partial \tau_3} &= \frac{\partial \dot{p}_{23}}{\partial t_2}\frac{\mathrm{d}t_2}{\mathrm{d}t_3}\frac{\mathrm{d}t_3}{\mathrm{d}\tau_3} + \frac{\partial \dot{p}_{23}}{\partial t_3}\frac{\mathrm{d}t_3}{\mathrm{d}\tau_3}.
\end{aligned} \tag{E.8}$$

Derivatives of different timescales can be found in equations (E.5) and (E.6). Remaining terms of equation (E.8) can be expanded as

$$\begin{aligned}
\frac{\partial \dot{p}_{12}}{\partial t_1} &= +\frac{1}{r_{12}^3}(\mathbf{r}_{12}\cdot\dot{\mathbf{r}}_1)(\mathbf{r}_{12}\cdot\dot{\mathbf{r}}_1) - \frac{1}{r_{12}}(\dot{\mathbf{r}}_1\cdot\dot{\mathbf{r}}_1 - \mathbf{r}_{12}\cdot\ddot{\mathbf{r}}_1) \\
\frac{\partial \dot{p}_{12}}{\partial t_2} &= -\frac{1}{r_{12}^3}(\mathbf{r}_{12}\cdot\dot{\mathbf{r}}_2)(\mathbf{r}_{12}\cdot\dot{\mathbf{r}}_1) + \frac{1}{r_{12}}(\dot{\mathbf{r}}_2\cdot\dot{\mathbf{r}}_1) \\
\frac{\partial \dot{p}_{23}}{\partial t_2} &= +\frac{1}{r_{23}^3}(\mathbf{r}_{23}\cdot\dot{\mathbf{r}}_2)(\mathbf{r}_{23}\cdot\dot{\mathbf{r}}_2) - \frac{1}{r_{23}}(\dot{\mathbf{r}}_2\cdot\dot{\mathbf{r}}_2 - \mathbf{r}_{23}\cdot\ddot{\mathbf{r}}_2) \\
\frac{\partial \dot{p}_{23}}{\partial t_3} &= -\frac{1}{r_{23}^3}(\mathbf{r}_{23}\cdot\dot{\mathbf{r}}_3)(\mathbf{r}_{23}\cdot\dot{\mathbf{r}}_2) + \frac{1}{r_{23}}(\dot{\mathbf{r}}_3\cdot\dot{\mathbf{r}}_2).
\end{aligned} \tag{E.9}$$

By substituting equations (E.5)–(E.9) into (E.7) we can get the expansion of $1/c^2$ terms of equation (E.1).

Formally, the second derivative of phase can be written as

$$\frac{\mathrm{d}^2\phi}{\mathrm{d}\tau_3^2} = \frac{\mathrm{d}F_R}{\mathrm{d}\tau_3}(\mathbf{r}_i,\dot{\mathbf{r}}_i,\ddot{\mathbf{r}}_i)\Big|_{o(1/c)} + \frac{\mathrm{d}F_R}{\mathrm{d}\tau_3}(\mathbf{r}_i,\dot{\mathbf{r}}_i,\ddot{\mathbf{r}}_i)\Big|_{o(1/c^2)}. \tag{E.10}$$

[12] The last two terms are very small($\simeq 10^{-10}$) and will be ignored.

Here the scale of station time τ_3 is the same as time tag of the data block. So the phase derivatives are equal to each other:

$$\frac{\mathrm{d}^2\phi}{\mathrm{d}\tau_3^2} = \frac{\mathrm{d}^2\phi}{\mathrm{d}t^2}. \tag{E.11}$$

E.2. Magnitude estimation of $\frac{\mathrm{d}^2\phi}{\mathrm{d}\tau_3^2}$ with the case of MEX mission

Considering a common three-way tracking of MEX with the uplink station of New Norcia located in Australia and the downlink station of Sheshan located in China:

- Distance from station to MEX: $r_{12} \simeq r_{23} = 2\times10^8$ Km.
- Distance between stations: $r_{13} \simeq 3000$ Km.
- Velocity of station relative to SSB: $\dot{r}_1 \simeq \dot{r}_3 = 30$ Km s^{-1}.
- Velocity of MEX relative to SSB $\dot{r}_2 \simeq 30$ Km s^{-1}.

Considering that the distance between station and spacecraft is much larger than the distance between stations, the following relationship is defined and established:

$$\begin{aligned}
\hat{\mathbf{e}} &= \frac{\mathbf{r}_{23}}{r_{23}} \\
&\simeq -\frac{\mathbf{r}_{12}}{r_{12}}.
\end{aligned} \tag{E.12}$$

Here, $\hat{\mathbf{e}}$ is the unit vector of the opposite direction of line-of-sight.

The first order of equation (E.10). By ignoring the influence of gravitation on the timescale derivative (equation (E.5)), the first order of equation (E.10) can be simplified as

$$\begin{aligned}
\frac{\mathrm{d}F_R}{\mathrm{d}\tau_3}(\mathbf{r}_i,\dot{\mathbf{r}}_i,\ddot{\mathbf{r}}_i)\Big|_{o(1/c)} \simeq -\frac{M_2 F_T}{c}\Big[&(\delta_{12}^1 + \hat{\mathbf{e}}\cdot\ddot{\mathbf{r}}_1)(1-\beta_v) \\
&+ (\delta_{12}^2 + \delta_{23}^2 - 2\hat{\mathbf{e}}\cdot\ddot{\mathbf{r}}_2)(1-\beta_u) \\
&+ (\delta_{23}^3 + \hat{\mathbf{e}}\cdot\ddot{\mathbf{r}}_3)\Big].
\end{aligned} \tag{E.13}$$

In the equation amplitude of $\ddot{\mathbf{r}}_1$ and $\ddot{\mathbf{r}}_3$ in the frame of SSB is about 10^{-2} m s^{-2} due to Earth rotation and the amplitude of $\ddot{\mathbf{r}}_2$(MEX) is about 1 m s^{-2} due to orbit motion. δ_{ij}^i are cross velocity terms with the dimension of acceleration and with amplitude of 10^{-3} m s^{-2}:

$$\begin{aligned}
\delta_{12}^1 &= +\frac{1}{r_{12}^3}(\mathbf{r}_{12}\cdot\dot{\mathbf{r}}_1)(\mathbf{r}_{12}\cdot\dot{\mathbf{r}}_{12}) - \frac{1}{r_{12}}(\dot{\mathbf{r}}_1\cdot\dot{\mathbf{r}}_{12}) \\
\delta_{12}^2 &= -\frac{1}{r_{12}^3}(\mathbf{r}_{12}\cdot\dot{\mathbf{r}}_2)(\mathbf{r}_{12}\cdot\dot{\mathbf{r}}_{12}) + \frac{1}{r_{12}}(\dot{\mathbf{r}}_2\cdot\dot{\mathbf{r}}_{12}) \\
\delta_{23}^2 &= +\frac{1}{r_{23}^3}(\mathbf{r}_{23}\cdot\dot{\mathbf{r}}_2)(\mathbf{r}_{23}\cdot\dot{\mathbf{r}}_{23}) - \frac{1}{r_{23}}(\dot{\mathbf{r}}_2\cdot\dot{\mathbf{r}}_{23}) \\
\delta_{23}^3 &= -\frac{1}{r_{23}^3}(\mathbf{r}_{23}\cdot\dot{\mathbf{r}}_3)(\mathbf{r}_{23}\cdot\dot{\mathbf{r}}_{23}) + \frac{1}{r_{23}}(\dot{\mathbf{r}}_3\cdot\dot{\mathbf{r}}_{23}).
\end{aligned} \tag{E.14}$$

The definition of β factor(amplitude is about 10^{-4}):

$$\begin{aligned}
\beta_u &= \frac{\dot{r}_{23}}{c} \\
\beta_v &= \frac{\dot{r}_{12}+\dot{r}_{23}}{c}.
\end{aligned} \tag{E.15}$$

If we ignore the contributions of δ_{ij}^{i} and β, equation (E.13) can be further simplified as (in Newtonian frame):

$$\frac{\mathrm{d}F_R}{\mathrm{d}\tau_3}(\mathbf{r}_i,\dot{\mathbf{r}}_i,\ddot{\mathbf{r}}_i)\Big|_{o(1/c)} \simeq -\frac{M_2F_T}{c}[\hat{\mathbf{e}}\cdot\ddot{\mathbf{r}}_1 - 2\hat{\mathbf{e}}\cdot\ddot{\mathbf{r}}_2 + \hat{\mathbf{e}}\cdot\ddot{\mathbf{r}}_3]. \tag{E.16}$$

Here we can see that in Newton frame the second derivative of phase could be approximated as a function of line-of-sight acceleration of $\ddot{\mathbf{r}}_1, \ddot{\mathbf{r}}_2$ and $\ddot{\mathbf{r}}_3$ with an error of 10^{-3}m s^{-2}.

The second order of equation (E.10).The second order[13] of equation (E.10) can be simplified to the order of β^2:

$$\begin{aligned}\frac{\mathrm{d}F_R}{\mathrm{d}\tau_3}(\mathbf{r}_i,\dot{\mathbf{r}}_i,\ddot{\mathbf{r}}_i)\Big|_{o(1/c^2)} \simeq -\frac{M_2F_T}{c}\{&(1-\beta_v)\\ &\times[(\beta_m+\beta_w)\hat{\mathbf{e}}\cdot\ddot{\mathbf{r}}_1+\beta_m\delta_{12}^{1}+\beta_w\delta_{1}^{12}]\\ &+(1-\beta_u)[-(\beta_m+\beta_n+\beta_u)\hat{\mathbf{e}}\cdot\ddot{\mathbf{r}}_2+\beta_m\delta_{12}^{2}+\beta_n\delta_{23}^{2}+\beta_u\delta_{2}^{23}]\\ &+[\beta_n\hat{\mathbf{e}}\cdot\ddot{\mathbf{r}}_3+\beta_n\delta_{23}^{3}]+\beta_w(1-\beta_u)\delta_{2}^{12}+\beta_u\delta_{3}^{23}\}.\end{aligned} \tag{E.17}$$

Here, δ_{ij}^{i} terms are defined in equation (E.14) and new definitions of β are (with the amplitude of 10^{-4}):

$$\begin{aligned}\beta_w &= \frac{\dot{r}_{12}}{c}\\ \beta_m &= \frac{\dot{p}_{12}-\dot{r}_{23}}{c}\\ \beta_n &= \frac{\dot{p}_{23}-\dot{r}_{12}}{c}\\ \beta_{u,v,w,m,n} &\simeq 10^{-4}.\end{aligned} \tag{E.18}$$

The main term of equation (E.17) approximates to $\beta \simeq 10^{-4}$ m s^{-2}.

ORCID iDs

Jianguo Yan https://orcid.org/0000-0003-2612-4776

References

[1] Asmar S and Renzetti N 1993 The deep space network as an instrument for radio science research *NASA STI/Recon Tech. Rep.* N **95** 21456

[2] Fjeldbo G, Kliore A, Seidel B, Sweetnam D T and Cain D 1975 The pioneer 10 radio occultation measurements of the ionosphere of Jupiter *Astron. Astrophys.* **39** 91–6

[3] Tyler G *et al* 1989 Voyager radio science observations of neptune and triton *Science* **246** 1466–73

[4] Hinson D *et al* 2018 An upper limit on plutos ionosphere from radio occultation measurements with new horizons *Icarus* **307** 17–24

[5] Kliore A J *et al* 2008 First results from the Cassini radio occultations of the titan ionosphere *J. Geophys. Res.* **113** A09317

[6] Kliore A, Nagy A, Cravens T, Richard M and Rymer A 2011 Unusual electron density profiles observed by Cassini radio occultations in Titan's ionosphere: effects of enhanced magnetospheric electron precipitation? *J. Geophys. Res.* **116** A11318

[7] Tellmann S, Pätzold M, Häusler B, Bird M K and Tyler G L 2009 Structure of the Venus neutral atmosphere as observed by the radio science experiment Vera on Venus Express *J. Geophys. Res.* **114** E00B36

[8] Konopliv A S, Miller J K, Owen W M, Yeomans D K, Giorgini J D, Garmier R and Barriot J-P 2002 A global solution for the gravity field, rotation, landmarks and ephemeris of Eros *Icarus* **160** 289–99

[9] Rappaport N J, Iess L, Tortora P, Anabtawi A, Asmar S W, Somenzi L and Zingoni F 2007 Mass and interior of enceladus from Cassini data analysis *Icarus* **190** 175–8

[10] Iess L, Rappaport N J, Tortora P, Lunine J, Armstrong J W, Asmar S W, Somenzi L and Zingoni F 2007 Gravity field and interior of rhea from Cassini data analysis *Icarus* **190** 585–93

[11] Mackenzie R, Iess L, Tortora P and Rappaport N 2008 A non-hydrostatic rhea *Geophys. Res. Lett.* **35** L05204

[12] Dehant V *et al* 2009 Lander radioscience for obtaining the rotation and orientation of Mars *Planet. Space Sci.* **57** 1050–67

[13] Iess L, Rappaport N J, Jacobson R A, Racioppa P, Stevenson D J, Tortora P, Armstrong J W and Asmar S W 2010 Gravity field, shape and moment of inertia of Titan *science* **327** 1367–9

[14] Iess L, Jacobson R A, Ducci M, Stevenson D J, Lunine J I, Armstrong J W, Asmar S W, Racioppa P, Rappaport N J and Tortora P 2012 The tides of titan *Science* **337** 457–9

[15] Iess L *et al* 2014 The gravity field and interior structure of enceladus *Science* **344** 78–80

[16] Pätzold M *et al* 2016 A homogeneous nucleus for comet 67p/Churyumov–Gerasimenko from its gravity field *Nature* **530** 63

[17] Tortora P, Zannoni M, Hemingway D, Nimmo F, Jacobson R A, Iess L and Parisi M 2016 Rhea gravity field and interior modeling from Cassini data analysis *Icarus* **264** 264–73

[18] Folkner W *et al* 2017 Jupiter gravity field estimated from the first two Juno orbits *Geophys. Res. Lett.* **44** 4694–700

[19] Iess L *et al* 2018 Measurement of jupiters asymmetric gravity field *Nature* **555** 220

[20] Iess L *et al* 2019 Measurement and implications of Saturn's gravity field and ring mass *Science* **364** eaat2965

[21] Marouf E A, Tyler G L and Eshleman V R 1982 Theory of radio occultation by Saturn's rings *Icarus* **49** 161–93

[22] Zebker H A, Marouf E A and Tyler G L 1985 Saturn's rings: particle size distributions for thin layer models *Icarus* **64** 531–48

[23] French R G, Marouf E A, Rappaport N J and McGhee C A 2010 Occultation observations of Saturn's b ring and Cassini division *Astron. J.* **139** 1649

[24] Standish E M and Williams J G 1992 Orbital ephemerides of the Sun, Moon, and planets *Explanatory Supplement to the Astronomical Almanac* (Washington, DC: United States Naval Observatory) pp 279–323

[25] Folkner W M, Williams J G, Boggs D H, Park R S and Kuchynka P 2014 The planetary and Lunar ephemerides DE430 and DE431 *Interplanet. Netw. Prog. Rep.* **196** 1–81

[26] Jones D L, Folkner W M, Jacobson R A, Jacobs C S, Dhawan V, Romney J and Fomalont E 2014 Astrometry of Cassini with the VLBA to improve the Saturn ephemeris *Astron. J.* **149** 28

[27] Bertotti B, Iess L and Tortora P 2003 A test of general relativity using radio links with the Cassini spacecraft *Nature* **425** 374–6

[28] Armstrong J, Iess L, Tortora P and Bertotti B 2003 Stochastic gravitational wave background: upper limits in the 10–6 to 10–3 Hz band *Astrophys. J.* **599** 806

[13] Here $\frac{M_2F_T}{c}$ is treated as constant.

[29] Serra D, Di Pierri V, Schettino G and Tommei G 2018 Test of general relativity during the BepiColombo interplanetary cruise to Mercury *Phys. Rev.* D **98** 064059
[30] Armstrong J W 2006 Low-frequency gravitational wave searches using spacecraft Doppler tracking *Living Reviews in Relativity* **9** 1
[31] Lorell J and Sjogren W 1968 Lunar gravity: preliminary estimates from Lunar orbiter *Science* **159** 625–7
[32] Konopliv A, Binder A, Hood L, Kucinskas A, Sjogren W and Williams J 1998 Improved gravity field of the Moon from Lunar prospector *Science* **281** 1476–80
[33] Konopliv A S, Yoder C F, Standish E M, Yuan D-N and Sjogren W L 2006 A global solution for the Mars static and seasonal gravity, Mars orientation, Phobos and Deimos masses and Mars ephemeris *Icarus* **182** 23–50
[34] Lemoine F G, Smith D E, Rowlands D D, Zuber M, Neumann G, Chinn D and Pavlis D 2001 An improved solution of the gravity field of Mars (GMM-2B) from Mars global surveyor *J. Geophys. Res.* **106** 23359–76
[35] Hoffman J, Hodges R, Donahue T and McElroy M 1980 Composition of the Venus lower atmosphere from the pioneer Venus mass spectrometer *J. Geophys. Res.* **85** 7882–90
[36] Hanson W, Sanatani S and Zuccaro D 1977 The Martian ionosphere as observed by the Viking retarding potential analyzers *J. Geophys. Res.* **82** 4351–63
[37] Abbate S F *et al* 2003 The Cassini gravitational wave experiment *Gravitational-Wave Detection Proc. SPIE.* **4586** 90–8
[38] Sniffin R 2005 Dsms telecommunications link design handbook *Technical Report, JPL/NASA*
[39] Jensen B E 1998 New high performance integrated receiver/ranging/demodulator system for estrack *SpaceOps Japan*
[40] Highsmith D E 2002 The effect of USO stability on one-way Doppler navigation of the Mars reconnaissance orbiter *Technical Report*
[41] Aung M, Hurd W, Buu C, Berner J, Stephens S and Gevargiz J 1994 The block V receiver fast acquisition algorithm for the Galileo s-band mission *The Telecommunications and Data Acquisition Report* pp 83–114
[42] Løfaldli A and Birkeland R 2016 Implementation of a software defined radio prototype ground station for cubesats *Proc. ESA Small Satellites Systems and Services Symp. (Valletta, Malta)* vol 30
[43] Storn R 1995 Differential evolution-a simple and efficient adaptive scheme for global optimization over continuous spaces *Technical Report* International Computer Science Institute 11
[44] Moyer T D 2005 *Formulation for Observed and Computed Values of Deep Space Network Data Types for Navigation* vol 3 (New York: Wiley)
[45] Price K, Storn R M and Lampinen J A 2006 *Differential Evolution: a Practical Approach to Global Optimization* (Berlin: Springer)
[46] Price K J, Hanson P J and Whittle B J 1994 Stimulation by carbachol of Mucus gel thickness in rat stomach involves nitric oxide *Eur. J. Pharmacol.* **263** 199–202
[47] Storn R and Price K 1996 Minimizing the real functions of the ICEC'96 contest by differential evolution *Proc. IEEE Int. Conf. on Evolutionary Computation* (IEEE) pp 842–4
[48] Price K V 1997 Differential evolution versus the functions of the 2/sup ND/ICEO *Proc. 1997 IEEE Int. Conf. on Evolutionary Computation* (IEEE) pp 153–7
[49] Nickolls J and Buck I 2007 NVIDIA CUDA software and GPU parallel computing architecture *Microprocessor Forum*
[50] Rupp K 2013 CPU, GPU and MIC hardware characteristics over time (www.karlrupp.net/2013/06/cpu-gpu-and-mic-hardware-characteristics-over-time/)
[51] Hoberock J and Bell N 2010 Thrust: a parallel template library (http://github.com/downloads/thrust/thrust/Thrust:%20A%20Productivity-Oriented%20Library%20for%20CUDA.pdf)
[52] Jian N *et al* 2009 A digital open-loop Doppler processing prototype for deep-space navigation *Sci. China* G **52** 1849–57
[53] Zhu R-J *et al* 2011 The progress of modern chinese data acquisition system *Prog. Astron.* **2** 207–16
[54] Stocker A *et al* 2018 An X band radio channel model for propagation through the solar corona *Radio Sci.* **53** 1014–22
[55] Yuen J H 2013 *Deep Space Telecommunications Systems Engineering* (Berlin: Springer)
[56] Pätzold M and Häusler M 2000 MaRS: Mars express orbiter radio science *Mars Express: The Scientific Payload* vol 1240 pp 141–63
[57] Zhang S-J, Jian N-C, Li J-L, Ping J-S, Chen C-Y and Zhang K-F 2015 Ionospheric inversion of the Venus express radio occultation data observed by Shanghai 25 m and new Norcia 35 m antennas *Res. Astron. Astrophys.* **15** 1559
[58] Jian N-C, Yan J-G, Ping J-S, Barriot J-P and Rodriguez J A P 2019 A new method to determine the gravity field of small bodies from line-of-sight acceleration data *Res. Astron. Astrophys.* **19** 048
[59] Moyer T D 1971 Mathematical formulation of the double-precision orbit determination program (DPODP) *Technical Report 32-1527, 10 + 160* NASA, Jet Propulsion Laboratory, California Institute Technology, Pasadena, CA pp 1